Contents lists available at ScienceDirect

Marine and Petroleum Geology

ELSEVIER

Research paper

Novel 3D centimetre-to nano-scale quantification of an organic-rich mudstone: The Carboniferous Bowland Shale, Northern England

CrossMark

Lin Ma [a, *], Kevin G. Taylor [a], Peter D. Lee [b, c], Katherine J. Dobson [b, c, d], Patrick J. Dowey [a], Loic Courtois [b, c]

[a] School of Earth, Atmospheric, and Environmental Sciences, University of Manchester, Manchester, M13 9WJ, UK
[b] Manchester X-ray Imaging Facility, School of Materials, University of Manchester, Manchester, M13 9PJ, UK
[c] Research Complex at Harwell, Rutherford Appleton Laboratory, Harwell, Oxfordshire, OX11 0FA, UK
[d] Department of Earth and Environmental Sciences, Ludwig-Maximilians-Universität München, Germany

ABSTRACT

X-ray computed tomography and serial block face scanning electron microscopy imaging techniques were used to produce 3D images with a resolution spanning three orders of magnitude from ~7.7 μm to 7 nm for one typical Bowland Shale sample from Northern England, identified as the largest potential shale gas reservoir in the UK. These images were used to quantitatively assess the size, geometry and connectivity of pores and organic matter. The data revealed four types of porosity: intra-organic pores, organic interface pores, intra- and inter-mineral pores. Pore sizes are bimodal, with peaks at 0.2 μm and 0.04 μm corresponding to pores located at organic–mineral interfaces and within organic matter, respectively. These pore-size distributions were validated by nitrogen adsorption data. The multi-scale imaging of the four pore types shows that there is no connected visible porosity at these scales with equivalent diameter of 20 nm or larger in this sample. However, organic matter and clay minerals are connected and so the meso porosity (<20 nm) within these phases provides possible diffusion transport pathways for gas. This work confirms multi-scale 3D imaging as a powerful quantification method for shale reservoir characterisation allowing the representative volumes of pores, organic and mineral phases to be defined to model shale systems. The absence of connected porosity at scales greater than 20 nm indicates the likely importance of the organic matter network, and associated smaller-scale pores, in controlling hydrocarbon transport. . The application of these techniques to shale gas plays more widely should lead to a greater understanding of properties in the low permeability systems.

© 2016 The Authors. Published by Elsevier Ltd. This is an open access article under the CC BY license (http://creativecommons.org/licenses/by/4.0/).

1. Introduction

Organic-rich shales (>2% TOC) have long been recognised as the source rock for conventional reservoirs but have recently also become the focus for exploration as reservoirs in their own right (Bustin et al., 2008; Clarkson et al., 2012a; Rokosh et al., 2008). Typically exhibiting very low permeabilities (1 μD to 1 nD) (Britt, 2012; Clarkson et al., 2012b; Macbeth et al., 2011), direct hydrocarbon production from a shale reservoir is achieved through hydraulic fracture stimulation combined with horizontal drilling (Lu et al., 2014; Sondergeld et al., 2013). In the United States, total dry natural gas production increased by 35% from 2005 to 2013, and the growth resulted largely from the development of shale gas resources (EIA, 2015). In the UK, the Carboniferous Bowland Shale in northern England is considered a principal target for shale gas exploration with gas-in-place estimates of 822 tcf (P90), 1329 tcf (P50) and 2281 tcf (P10) (Andrews, 2013; De Pater and Baisch, 2011).

Before accurate estimates of in-place volumes and assessment of the commercial potential via the likely effectiveness of fracture stimulation can be made, an improved understanding of the pore systems, organic matter and mineral distributions is needed. This will allow a basis of understanding gas storage, transport mechanics and possible fracture preferences to be built. As a fundamental property in shale reservoirs, porosity has both scientific and economic implications. It could influence physical properties of reservoirs and accurate porosity measurement is critical in resource estimates (Bustin et al., 2008; Dong et al., 2013). However, the sub-

micron to nano-scale porosity and heterogeneous nature of shales makes accurate reservoir quality estimates challenging. Traditional optical and scanning electron microscopy (SEM) techniques can provide 2D images across a wide range of spatial resolutions from meso-scale to nano-scale, but cannot provide information on the shape and connectivity of pore networks in 3D. Other methods (e.g. mercury intrusion porosimetry (MIP), nitrogen adsorption, nuclear magnetic resonance spectroscopy) can provide quantitative measures of connected porosity, and the diameters of connected pore throats, but cannot provide information on total porosity or the morphology of pore networks and often provide only very limited information on non-connected pore structures (Ausbrooks et al., 1999; Zhang and Scherer, 2012).

As the global interest in unconventional reservoirs has increased, imaging the porosity has become important. X-ray computed tomography (XCT) is now being used to image at both millimetre-scale and micron-scale (Heath et al., 2011; Sakellariou et al., 2003; Wang and Reed, 2009), and some multi-scale methods have been explored in a range of geological systems, including carbonates (Khalili et al., 2012; Sok et al., 2010) and shales (Caplan et al., 2011; Loucks et al., 2009). However, pores in shales are often only a few nm in diameter (Ambrose et al., 2010; Bai et al., 2013; Borst, 1982; Curtis et al., 2010) therefore they cannot be imaged using X-ray tomography techniques alone which have a maximum feature resolution of currently ~150 nm. Other techniques need to be combined with XCT to provide adequate information on shale reservoirs, that are known to be heterogeneous over a large range of scales (Clarkson et al., 2013; Knackstedt et al., 2012). To quantify the microstructural and heterogeneity across multiple scales, we apply the latest X-ray tomographic imaging techniques combined with three-dimensional electron microscopy (3D-EM) on a typical sample of Namurian Bowland Shale from northern England. We produce 3D maps of the mineral, organic and porosity networks over a range of spatial resolutions from 7.7 μm to 6.7 nm, across three orders of magnitude. Through this image-based understanding of the microstructure and the heterogeneity, we develop a model of the porosity, organic matter and minerals for the Bowland Shale sample and discuss possible gas storage and transport mechanisms. Such an appreciation of technique applications will lead to an enhanced understanding in other globally important shale reservoirs.

2. Geological setting

The Carboniferous, Namurian aged organic-rich Bowland Shale is present across a large part of the central and northern UK (Fig. 1) (De Pater and Baisch, 2011; Waters et al., 2011). It comprises a variety of clastic and carbonate facies deposited under the influence of glacio-eustatic sea level controls and tectonic events (Gawthorpe, 1987). High TOC (>2%), moderate to high thermal maturity (1.1% < Ro < 3.5%), and brittle bulk behaviour (interbedded limestones) give this formation significant reservoir potential (Andrews, 2013). Here we focus on one sample from the Swinden borehole in the west of the Bowland Basin (Charsley, 1984) (Fig. 1), from a depth of 193 ft and with a high TOC (6.8 wt %). This sample falls within the transition between the oil window and gas window (Ro = 1.1%), as is the case for the key target horizons in the Bowland Shale being considered for shale gas exploration (Andrews, 2013). Whilst only one sample is presented in detail here, we demonstrate that the approach and observations presented here can be applied to design wider-scale analysis programmes.

3. Methodology

Optical and scanning electron microscopy (SEM) with energy-

dispersive X-ray spectroscopy (EDX) was used to analyse petrological and sedimentary characteristics on a polished thin section.

X-ray computed tomography (XCT) images were obtained at three different length scales (see Table 1) for the sample. XCT images are generated by acquiring a series of 2D "projections" where each projection is a radiographic image collected from a different angle. The sample is placed in the X-ray beam and is rotated 360° around a vertical axis collecting images at regular intervals. As each mineral phase has specific X-ray absorption characteristics, when the sample rotates and the mineral assemblage along the beam path varies, the total X-ray flux hitting each pixel on the detector varies (Hsieh, 2009; Ketcham and Carlson, 2001; Long et al., 2009; Wellington and Vinegar, 1987). Mathematical reconstruction algorithms are then applied to reconstruct a 3D image (Feldkamp et al., 1984), and the image volumes represent 3D absorption (density/mineralogy) maps. The data presented here were collected at the Manchester X-ray Imaging Facility (MXIF), the Corrosion and Protection Centre in University of Manchester, and at the Diamond Light Source synchrotron. The imaged samples at each scale were selected randomly in the specified volumes and specified sizes due to the high heterogeneity. The largest samples (a 1 cm cube) (Resolution scale 1 or R1) were imaged with a spatial resolution of 7.7 μm/voxel (a 3D equivalent of a pixel and the smallest unit of a volume data set) using X-ray tomography system (XT H 225, Nikon, Tokyo, Japan) (Table 1). 1 mm diameter samples were imaged on the Diamond–Manchester Beamline, Diamond Light Source with voxel resolutions of 0.5 μm (R2). Sub-micron imaging (~0.13 μm/voxel; R3) was achieved using a laboratory nano-tomography system (Xradia Ultra, Zeiss, Oberkochen, Germany), with samples of ~65 μm diameter which was prepared based on a 65 μm thick thin section. Ultramicrotomy was attempted in order to provide samples with ~65 μm diameter but failed because of the high brittleness of shale samples. 3D-EM was performed using a 3View (Gatan, FEI, Pleasanton, United States) ultra-microtome mounted inside the vacuum chamber of an SEM to enable fully automatic imaging of large specimen volumes at high resolution (Lang et al., 2011). Approximately 250 2D SEM images were acquired within plane resolutions of 49 nm (R4) and 7 nm (R5), with vertical slice spacing of ~49 nm and 15 nm, respectively.

The 3D EM slices required aligning and shearing for the first step, and then all images were processed using 3D non-local means filters (local neighbourhood pixel 5, similarity value 0.3) for tomography data and 2D non-local means filters (same parameters with 3D) for slice stack to reduce image noise. Edge-preserving smoothing filter (contrast 5, sigma 2) was used to eliminate small contrast variations within the all phases without losing their shapes and the voxels of each phase (non-clay minerals, clay minerals, organic matter and pores) identified and labelled using standard methods (Korfiatis et al., 2007; Landis and Keane, 2010; Stauber and Müller, 2008). The volume of each pore was measured by voxels in Avizo (Standard and Fire versions, FEI, Hillsboro, United States) product suite, and the equivalent diameter, shape, orientation and local pore number density of each pore calculated based on the equations below. Equivalent diameter (EqD) of individual pores, defined as the diameters of spheres that would give the same volume (Thomas and Clouse, 1990), was calculated as the equivalent circular diameter to represent the pore size using the equation: $EqD = \sqrt[3]{6/\pi V}$, where V is the volume of pore (Pabst and Gregorova, 2007). Pore shape was calculated by shape factor as (Youssef et al., 2007): Shape factor (compactness) $= S^3/(36\pi V^2)$. Local density was calculated by considering the number of neighbouring pores within a certain radius from the centre of each pore (Casertano and Hut, 1985) and the radius was confirmed after primary calculation, which was used to describe the topological factors of pores. Finally a network
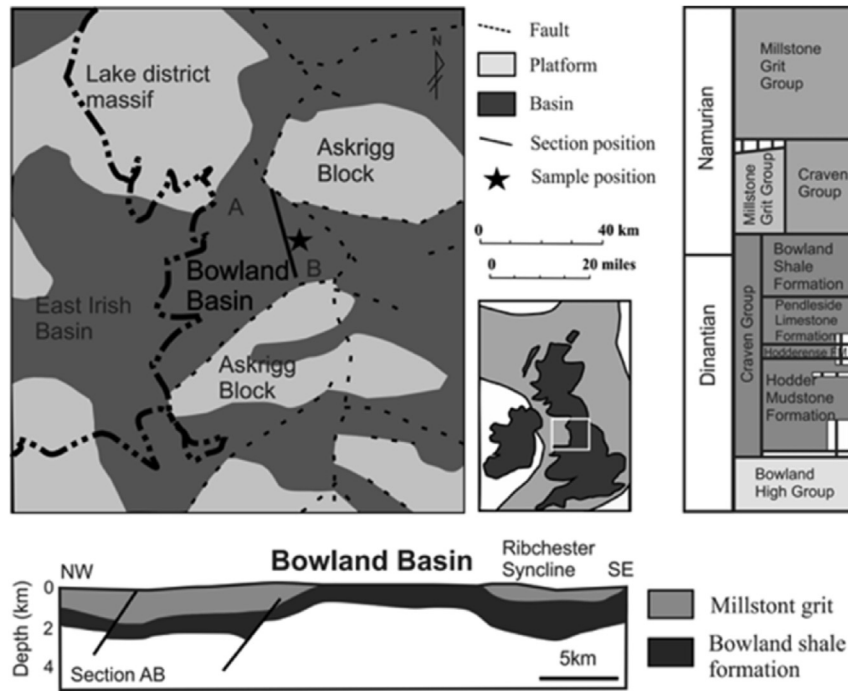
Fig. 1. The Bowland shale in the northern UK and sample location (after Andrews, 2013 and Waters et al., 2011).
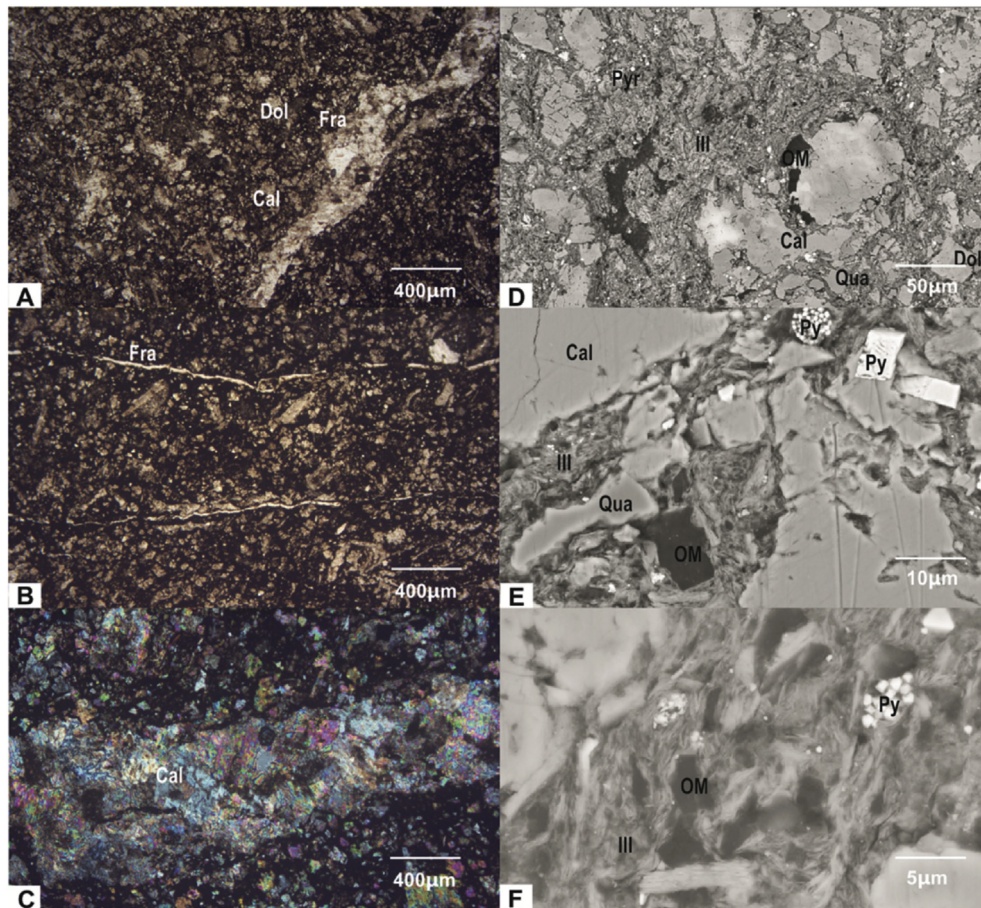

Fig. 2. Petrography of studied sample (thin section and SEM photomicrographs) (A, B and C- thin section photomicrographs; D, E, F- SEM photomicrographs) disrupted laminations in A and B; calcite (Cal), dolomites (Dol) and quartz (Qua) as main compositions shown in A, B, D and E; recrystallized calcite filling fractures (Fra) in A, B and C; matrix made up of sub-directional such as illite (Ill), amorphous organic matter (OM), and some heavy minerals such as pyrite (Py) and rutile, shown in D, E and F.

Table 1
Parameters for image acquisition from X-ray tomography and 3D-EM at R1-R5.

Methods	X-ray tomography			3D-EM	
Scales	Meso-scale (R1)	Micro-scale (R2)	Submicron-scale (R3)	Low-resolution nano-scale (R4)	High-resolution nano-scale (R5)
Sample size	1 cm	1 mm	100 μm	50 μm	14 μm
Spatial pixel size	7.7 μm	0.5 μm	130 nm	49 nm for X and Y, 50 nm for Z	6.7 nm for X and Y, 15 nm for Z
Energy (kV)	52	N/A	40	30	30
Current (mA)	0.299	N/A	30	N/A	
Filter	None	None	None		

analysis (connectivity, local thickness) of the porosity and organic matter was performed (Avizo, FEI, Figs. 3—6). Local thickness is defined as the diameter of the largest sphere that fits inside the object and contains the point (Hildebrand and Rüegsegger, 1997). Additionally, the segmentation errors have been considered for these images by left- and right-deviating 1 minimum unit in grayscale thresholding of each phase, and the quantified errors of the volume percentages are ±14%, ±6%, ±4% for the tomography images at R1, R2 and R3, and ±0.3% for 3D EM images at R4 and R5.

Representative elementary volume (REV) is defined as a minimum volume of the property field that is large enough to capture a representative amount of the heterogeneity (Bear and Braester,
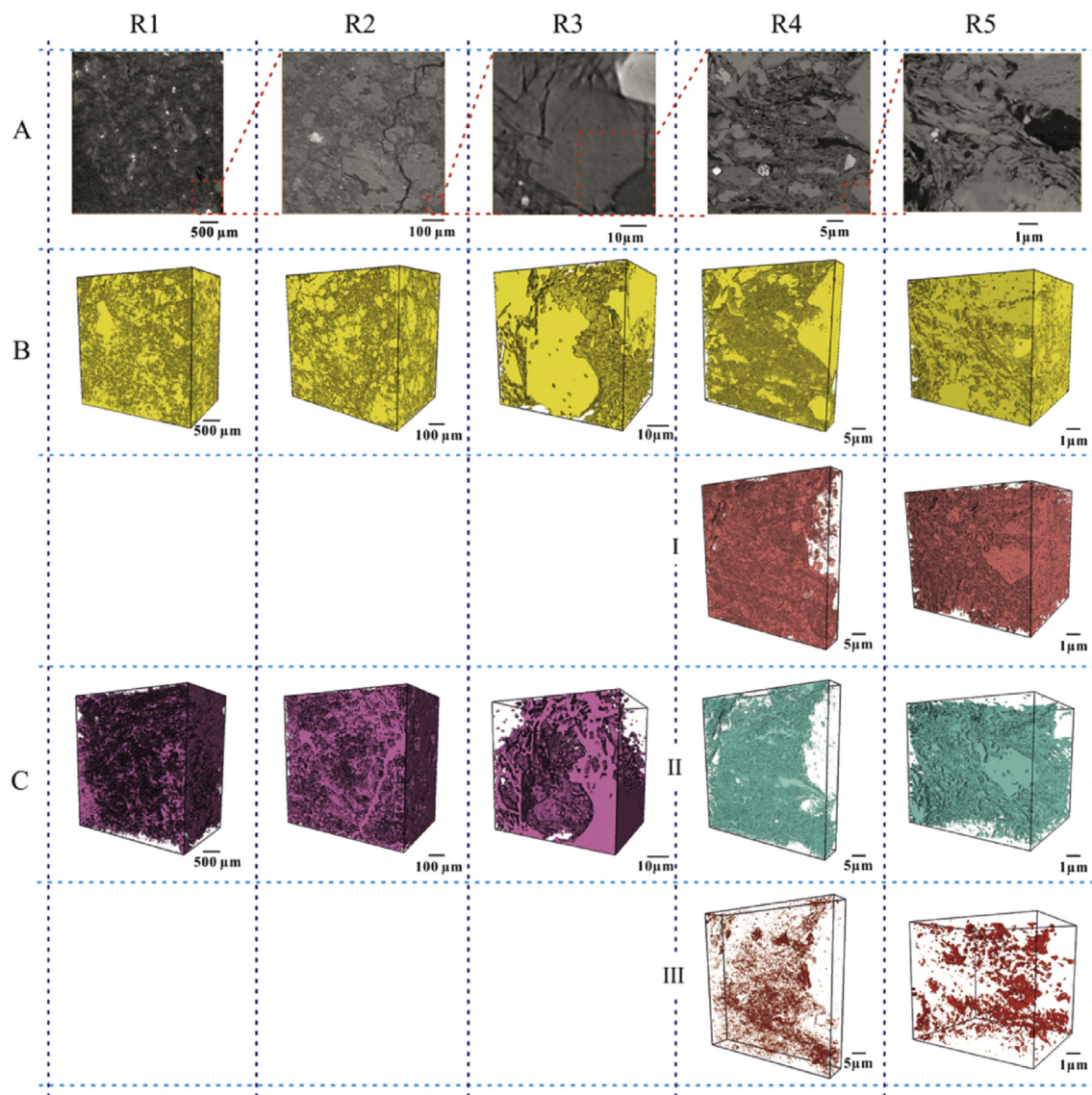

Fig. 3. Multi-scale images of the minerals, organic matter and pores. (Colours refer to different segmented phases. Images at R1—R3 are XCT images and images at R4—R5 are 3D-EM images.) (A) 2D slices from each of the data sets showing the typical structures observed (note the zoom in boxes fire relative scale. (B) A mixture of non-clay minerals including dolomite, calcite, quartz and pyrite (the non-clay minerals) which could be segmented at all resolutions. (C) R1, R2 & R3: it was not possible to separate the clay minerals, organic matter and pores, and the combined are therefore rendered together. R4 & R5: clay minerals (I), organic matter (II) and pores (III) were separable. Colors are showing Voxel resolutions for R1—R5 are described in the text, R1—R3 showing XCT images and R4—R5 showing 3D-EM images. (For interpretation of the references to colour in this figure legend, the reader is referred to the web version of this article).
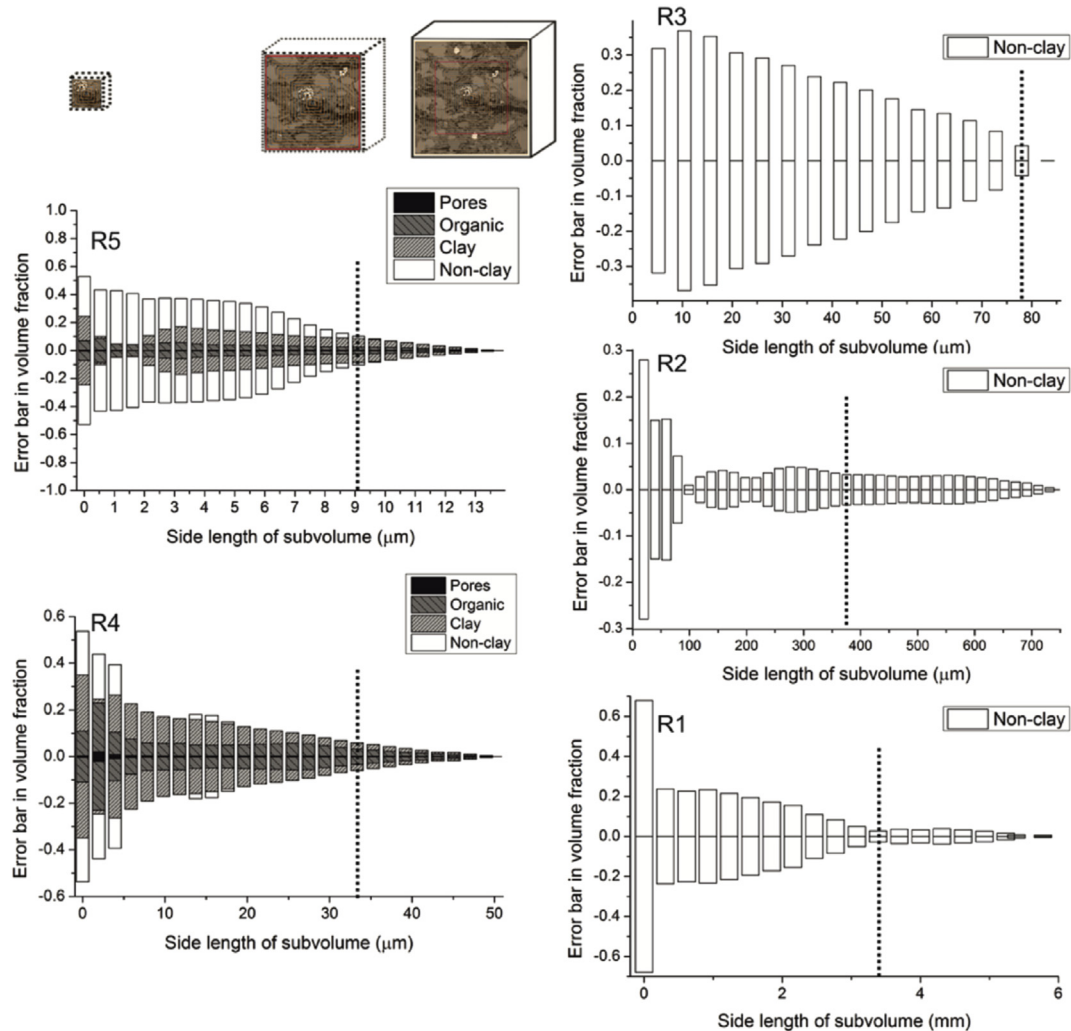
Fig. 4. Representative elementary volume (REV) at R1—R5, volume fractions of non-clay minerals, clay minerals, organic matter and pores shown at R5 and R4, volume fractions of non-clay minerals, combined material including clay minerals, organic matter and pores shown at R1, R2 and R3, vertical dash lines showing the left boundaries of REV. Maximum samples sizes at five scales are all larger than the REV, showing that the selected samples are representative at corresponding scales.

1972; Gitman et al., 2007). It was performed at each scale to find out the minimum representative sample size for the typical features resolved at this scale. The subvolume sizes on the 3D images started using the entire volume at each scale and were then decreased by 40 pixels in each dimension towards five stochastic centroids, and the volume fractions of segmented phases in decreasing subvolumes was calculated. The errors in volume fraction compared with the average fractions were calculated at each step based on these stochastic centroids and plotted in Fig. 4. The connectivity and distribution of organic matter was also measured. Connectivity was measured along three orthometric directions: parallel to bedding (the Z axis), and vertical to bedding (the X and Y axes). The spatial distribution was determined using a skeletonisation algorithm which defined the centre line of the organic network, which was then abstracted into nodes and tube segments with thickness scaled by the size and shape of the local organic structure (Youssef et al., 2007).

To validate the image-based phase and pore quantification, several laboratory analyses were undertaken. Nitrogen adsorption was measured using a surface area analyser (ASAP 2020, Micromeritics, Norcross, United States) and pore size distribution determined using the Brunauer–Emmett–Teller (BET) method. These data were compared to pore size distributions extracted from 3D

images. Total organic carbon (TOC) was determined using a carbon analyser (Leco, Michigan, United States) after rock acidification and organic matter combustion with a possible error ± 0.02%. X-ray Diffraction (Bruker D8Advance XRD, Billerica, United States) was used to confirm the mineralogy and identify the clay phases present in the sample with a possible volume error ± 1%. The volume percentage of organic matter and minerals calculated from the TOC and XRD measurements by considering specific densities were comparable to those used for the X-ray tomography/3D-EM.

4. Results

4.1. Multi-scale mineralogy and microstructure

Thin section observations show that the sample is composed of disrupted laminations with calcite, dolomite, detrital clay minerals, quartz and organic matter, and some fine and discrete fractures filled with calcite (Fig. 2 A, B and C). Backscatter SEM observations (Fig. 2 D, E and F) of a polished thin section reveal that authigenic crystalline calcite, detrital calcite, dolomite and quartz are major components, and the matrix contains irregular organic matter pieces and clay minerals especially fibrous illites. Some pyrite occurs as isolated crystals while others form 1—5 μm size framboids.
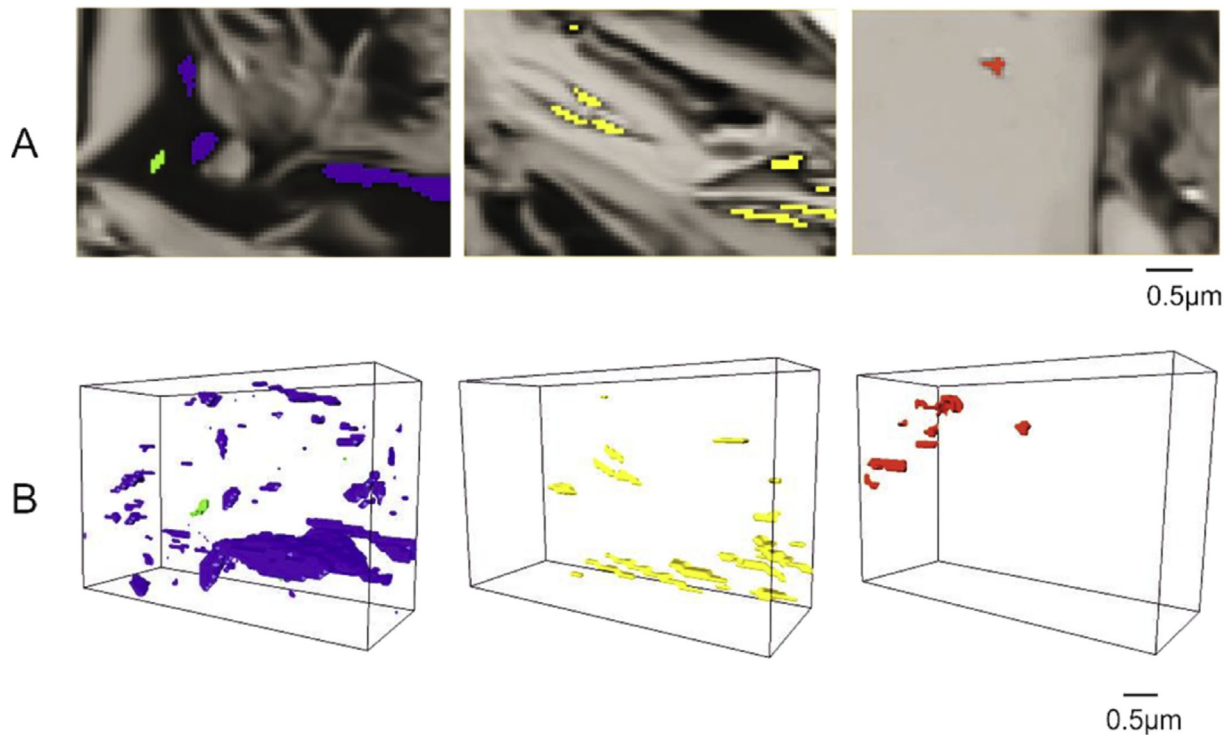
Fig. 5. 2D images and 3D renders of the different pore types at R4 and R5 (A) 2D slices of the 3D-EM dataset with coloured four pore types, blue: organic matter interface pores, referring to pores lying at the interface of organic matter and minerals, green: intra-organic pores, referring to pores organic matter bounded pores, yellow: inter inorganic pores, referring to pores lying between inorganic minerals, red: intra mineral pores, referring to pores totally bonded in mineral grains (B) corresponding 3D volume rendering of different pores types. (For interpretation of the references to colour in this figure legend, the reader is referred to the web version of this article).
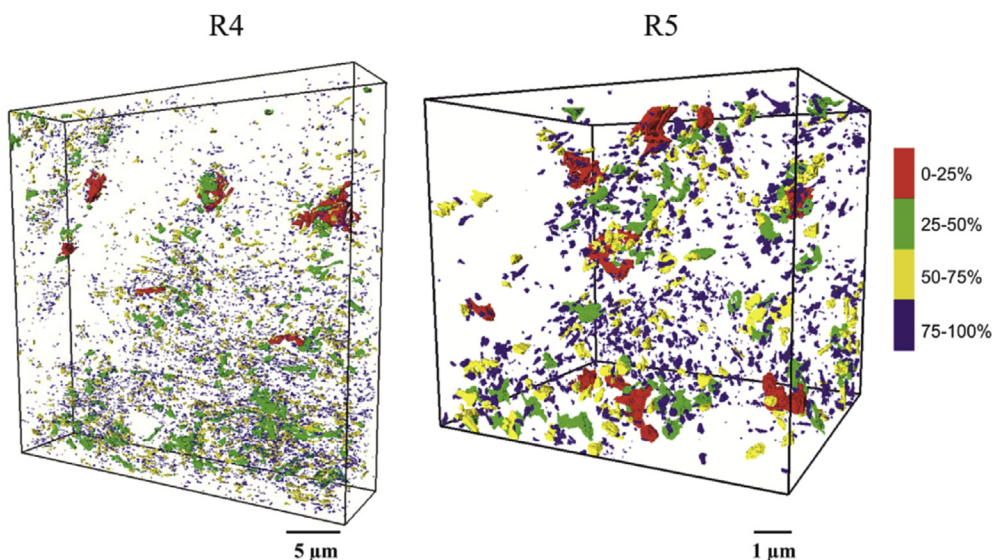

Fig. 6. Pore classification by volume for 3D volumes at R4 and R5, showing volume quartiles distribution pores classified by quartered volume.

The TOC, EDX and XRD analysis of the sample defined a mineralogy of dolomite, calcite, illite, kaolinite, quartz, and pyrite for this sample (Table 2) which had TOC of 6.83 ± 0.02 wt %. These weight percentages have been recalculated as volume percentages based on the densities (Table 2).

The lowest resolution 3D image at 7.7 μm/voxel (R1, XCT, Fig. 3) reveals little about the mineralogical or structural variability of this sample. Although there is some evidence for local greyscale (mineralogy/density) variability, probably caused by differences in the local mineral phases and total mineral content, it cannot be used to quantify phase distributions. The lack of microstructural information at R1 is caused by the small particle sizes. Each voxel in the 3D image contains more than one phase, therefore there is a high degree of averaging showing the average greyscale value of the phases. It is not possible to observe any but the largest fractures at this resolution. Specifically, some calcite filled fractures above 20 microns could be segmented and have been merged into non-clay minerals as part of calcite (Fig. 3B). In shale samples where there is

Table 2
TOC corrected weight percentages and calculated volume percentages of minerals and organic matter.

Mineral phases	Weight percentage (wt %)	Mixed phase	Weight percentage (wt %)	Volume percentage (vol %)
Dolomite	27	Non-clay minerals	68	63
Calcite	25			
Quartz	14			
Pyrite	2			
Illite	23	Clay minerals	35	23
Kaolinite	2			
TOC	7	Organic matter	7	14

substantial mineralogical heterogeneity on the mm (lamination) scale, R1 image resolution may yield information about the bulk mineralogical variability, but the Bowland Shale sample in this study was too homogenous for semi-quantitative analysis at this scale. It should also be noted that scanning at still lower resolutions was also undertaken with the resolution of 100 microns (10 cm cores were tested) but showed no mineralogical or structural information and is therefore not included here.

At higher resolution (R2, 1.3 μm/voxel; R3, 0.13 μm/voxel, both XCT, Fig. 3) the sample shows disrupted laminations with some discrete calcite-filled fine fractures. The matrix is made up of clay minerals and organic matter (Fig. 3A). The quantitative image analysis reveals the non-clay minerals (carbonates and pyrite) and the lower X-ray attenuating material (clay minerals, organic matter and pores) to be 32 ± 6 vol % and 68 ± 6 vol% respectively at R2, and 36 ± 4 vol% and 64 ± 4 vol% at R3. The data, therefore, show good agreement with the XRD/TOC data and between the R2 and R3 resolutions. The organic matter is a key element controlling gas generation and adsorbed gas storage in shale reservoirs; however, imaging the organic material is challenging at R2 and R3 because of low attenuation contrast between the organic matter and clay phases, and the volume averaging effect of sub-voxel scale mixed mineralogy.

At the highest resolution images (R4, 50 nm/voxel; R5, 6.7 nm/voxel, both 3D-EM, Fig. 3), the equant grains of quartz and carbonates grains account for 49 ± 0.3 vol % at R4 and 61 ± 0.3 vol % at R5. At these resolutions the clay minerals and the organic matter can be separated, and randomly orientated fibrous illite makes up 32 ± 0.3 vol % at R4 and 24 ± 0.3 vol % at R5. There is also good correlation between the non-clay minerals (mainly including calcite, dolomite, quartz and pyrite which were identified by grey values and geometry) and clay minerals (mainly including illite and kaolinite) volume fractions measured from image analysis and the XRD analysis of volumes. The clay minerals themselves are also highly connected (97% and 98% at R4 and R5, Fig. 3 C-R4 and R5). The organic matter makes up 10 ± 0.3 vol % at R4, and 12 ± 0.3 vol % at R5. The relative volumes of the different phases varies more between R4 and R5 than seen at lower resolution, but this minor inter-sample variability is to be expected as shales are inherently heterogeneous. At R4 and R5 it is also possible to observe and quantify the porosity. Pores make up 0.52 ± 0.3 vol % at R4 and 0.55 ± 0.3 vol % at R5. 3D renders of the organic matter and pore volumes at R4 and R5 are shown in Fig. 3.

Based on the multi-scale imaging results, the appropriate scales of specified phases were analysed systematically according to the field of view and spatial resolution which represent the maximum and minimum visual sizes of images at each scale. Pores, organic matter and clay minerals can be observed at only R4 and R5 resolutions due to the low spatial pixel sizes (Fig. 3C), and the limitation of the field of view below 50 μm at these two scales makes the distribution and quantification of non-clay minerals not possible (Fig. 3B).

The minimum representative sample sizes were analysed by the approach of representative elementary volumes (REV), and the variation of REVs at R1–R5 shows the multi-scale heterogeneity (Fig. 4, Table 3). The organic matter and pores are only discriminated at R4 and R5 resolutions, and the REVs are 1500 voxels at R5, which corresponds to ~10 μm edge length cube, and 680 voxels for 33 μm at R4. When clay mineral and non-clay mineral are considered, the REVs at R3, R2 and R1 are corresponding to 78 μm, 380 μm and 3.4 mm respectively.

4.2. Pore volume analysis

More detailed assessment of the porosity shows that four pore types can be identified based on the geometry, and the relationship with mineral/organic matter (Fig. 5, Table 4): i) intra-organic matter pores, relatively small (typically < 0.2 μm diameter) spherical pores bounded in organic matter particles, ii) organic matter interface pores, generally larger, irregular and curved pores (0.2–2 μm diameter) at the interface between the organic matter and mineral phases, iii) inter-mineral pores, elongated pores at the grain boundaries between mineral phases (0.2–1 μm diameter), and iv) intra-mineral pores, elliptical or angular pores (0.05–0.3 μm) bounded in calcite, dolomite or quartz particles.

To assess the pore volume distribution, pores were split into four groups with quartiles of total volume by the equivalent diameters in decreasing order (Fig. 6). Pores with an equivalent diameter above 0.21 μm make up the upper quartile. These are scattered through the whole sample and have irregularly curved surfaces. The pores in second (EqD = 0.13–0.21 μm) quartile are generally elongated between minerals, whereas in the third quartile (EqD = 0.11–0.13 μm) the pores are scattered along the bedding direction and have more spherical shapes. The fourth quartile (EqD < 0.11 μm) is dominated by a spherical or ellipsoidal geometry inside organic matter or minerals (intra-organic and intra-mineral pores). The dominant pore types in the larger two groups (red and green in Fig. 6) show higher degrees of elongation corresponding to organic matter interface pores (type ii) and inter-mineral pores (type iii) respectively, while the smaller two groups (yellow and blue in Fig. 6) correspond to the intra-particle pores including intra-organic matter pores and intra-mineral pores.

The preliminary result of the computed distance between every two neighbours suggests that a majority of pores have at least one neighbour in a sphere of 1 μm radius at R5 or 5 μm at R4, which is used as to be the radius distance for the local density measurements. Applying a similar classification method with pore volume distribution to the calculated local density data of pores (Fig. 7) shows that the maximum number of neighbours (MNN) for R4 is 55 and rises to 133 at R5. The 0–25% pore group shows a higher density of 100–133 MNN per sphere and at R5, the 75%–100% grouping has 0–33 MNN per sphere. The large pores in the top 25% volume appear to always have a lower density due to the large diameters, and the local densities of other pores in 25%–100% volume depend on the positions and the relationship of organic

Table 3
Representative elementary volume (REV) results and corresponding voxels at R1–R5.

Scales	Meso-scale (R1)	Micro-scale (R2)	Submicron-scale (R3)	Low-resolution nano-scale (R4)	High-resolution nano-scale (R5)
REV	3.4 mm	380 μm	78 μm	33 μm	10 μm
Corresponding voxels	440 voxels	760 voxels	600 voxels	680 voxels	1500 voxels

Table 4
Summary of four pore types.

| Pore type	Location	Shape	Size
Intra-organic matter pores	Present in organic matter particles	Spherical	<0.2 μm diameter
Organic matter interface pores	At the interface between the organic matter and mineral phases	Irregular and curved	0.2–2 μm diameter
Inter-mineral pores	At the grain boundaries between mineral phases	Elongated	0.2–1 μm diameter
Intra-mineral pores	Present in calcite, dolomite or quartz particles	Elliptical or angular pores	0.05–0.3 μm
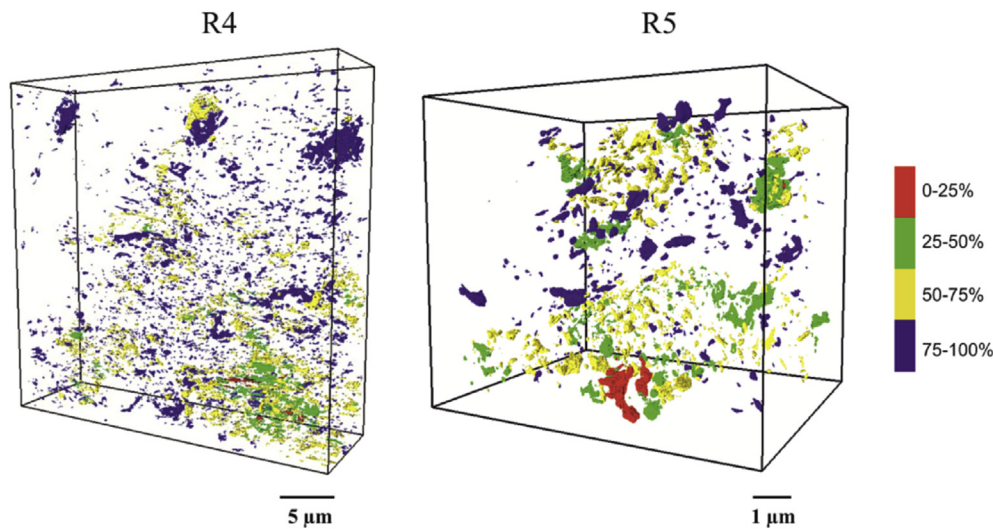
Fig. 7. Pore classification by local density for 3D volumes at R4 and R5. Pores classified by number of neighbours in a 1 μm sphere from individual pore centre (colours relate to those in Fig. 3 but with value in number of neighbours). (For interpretation of the references to colour in this figure legend, the reader is referred to the web version of this article).

matter. Pores with high local density tend to be close to the organic matter surface, including organic matter interface pores and inter-mineral particle pores, which means these pores are likely to form connections more easily during stimulation processes including heating and hydraulic fracturing. The lower density often lies with intra-organic and intra-mineral pores, which are both inside particles and not easy to get through.

The pore size distribution measured by nitrogen adsorption and binned by diameter shows a bimodal distribution with a major peak at 0.04 μm and a minor peak at 0.2 μm (Fig. 8A). These correlate well to the pore-size distribution curves obtained from image analysis (Fig. 8A) where R5 shows the same bimodal distribution, and R4 resolves only the larger pores. The 3D data allow total pore volume to be assessed, and volume fractions of pores with the same bins in diameter are measured to present their volume contribution by diameters. The curves show that although the smaller pores (around the major peak in diameter, 0.04 μm), mainly made up of intra-organic pore and intra-mineral pores, are more prevalent in number, they make only a small contribution to the total pore volume fraction (Fig. 8B). The rare large, inter-particle pores (around the minor peak in diameter, 0.2 μm), especially those at the organic matter interface (types iii and iv) dominate the total volume. The pore orientations (directions of long axes) were analysed based on the plane parallel to the upper surface (0–360° in XY plane) and normal to upper surface (0–90 in Z direction). The

bedding plane is clearly identified as around 60° in Z direction. There is no strong pore orientation in the XY plane (left in Fig. 8C), with only a minor drop in the range of 50–70° in the Z direction, roughly parallel to the bedding plane (right in Fig. 8C). The scatter plot (Fig. 8D) graph of equivalent diameter and shape factor shows that most of the pores in the 0.03–0.08 μm range are near spherical or elliptic and at diameters above 0.08 μm are more elongated in shape.

4.3. Organic matter distribution

The organic matter cannot be distinguished from clays in R1 to R3, but at R4 and R5 the volume percentage measured from the images agrees well with the measured TOC (~7 wt %, ~13 vol%). The connectivity of the organic matter was tested through three orthometric directions and the connectivity parallel to bedding is presented here as the highest value (along the z axis, Fig. 9): 79.0% at R4 and 78.2% at R5. The consistency of organic connectivity indicates the spatial pixel size is not considered to be the primary affecting factor for organic matter connectivity (Fig. 9A). A skeletonisation based on the centre line of the organic network is presented in Fig. 9, and tubes of each branch from the skeleton are shown with local thickness values to give a clear view of organic matter distribution (Fig. 9B). Organic matter was then binned by local thickness and plotted as a scatter diagram with local thickness
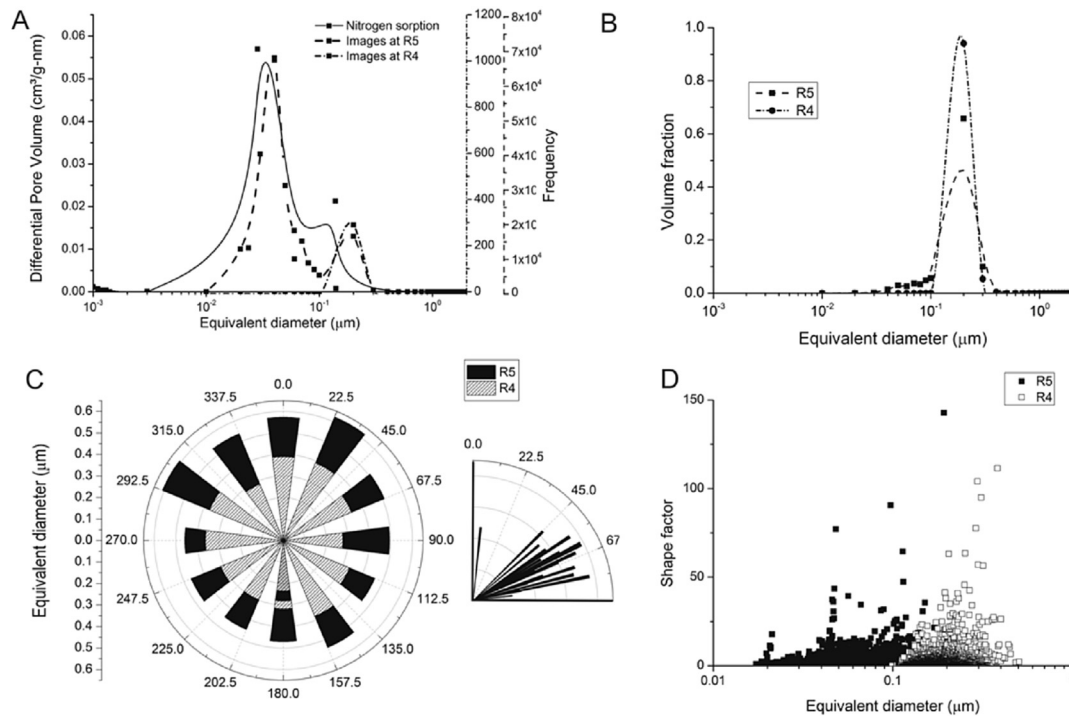
Fig. 8. Pore analysis by nitrogen adsorption and 3D imaging. A) Pore diameter distribution from nitrogen adsorption (solid curve) and the image analysis data at R5 (dash) and R4 showing similar trends (the ~0.2 μm pores can be observed at both resolutions, the smaller ~0.05 μm pores are only visible at R5). B) Image analysis results as a function of volume fraction. C) Rose diagram showing pore orientation data (left-thera, 0—360°, right-phi, 0—90°). D) Scatter diagram of pore geometry showing the smaller pores are generally the more spherical (filled — R4, open -R5), shape factors calculated from $S^3/(36\pi V^2)$.

and frequency (Fig. 9C). The statistical data shows the maximum value of local thickness is 1.75 μm for R4 and 0.65 μm for R5, and the frequencies decrease in overall trends along with some slight fluctuates when local thickness increases.

5. Discussion

5.1. The representative nature of the multi-scale data

The high heterogeneity and the extremely fine grain-size of shales require images over a large range of resolutions, and utilising four kinds of XCT and 3D-EM techniques in this study has built a picture of the Bowland Shale sample across three orders of magnitude from the meso-to nano-scale in 3D view (7.7 μm—6.7 nm). Although a few studies of 3D imaging studies in other shale reservoirs have considered a few scales of observations (Clarkson et al., 2013; Knackstedt et al., 2012), none has been comprehensive. The results of our imaging show that different scales of observations are needed for different mineral or textural discrimination, (i) meso-scale to micro-scale images elucidate the geometry of sedimentary layering and fractures; (ii) micron-to submicron-scale can discriminate the morphology and distribution of non-clay minerals and organic matter; and (iii) nano-scale resolution reveals the pore system, organic-matter connectivity and fine-grained clay mineral matrix. The combination of XCT and 3D-EM reduces the limitations of minimum resolution for X-ray tomography and the maximum view field for 3D-EM in shale reservoirs. Image analysis allows the quantification of individual pores/organic matter/minerals including diameters, volumes, shapes, thickness and orientations and also the topological factors of the network such as connectivity and local density, and these values can be used for building the spatial distribution or further analysis.

The representivity of the multi-scale imaging undertaken here can also be considered. Due to the highly heterogeneous nature of shales, the smallest representative volumes shown in REV (Fig. 4) differ with scales, and the spatial resolution and the field of view should be systematically considered to optimize the visualization of the features. For example, organic matter, clay minerals and pores are best observed at R4 and R5 resolutions so sample sizes should be between 9 and 38 μm (REV values at R4 and R5) while the larger features such as non-clay minerals are clearly seen above R3 and may require sample sizes above 49 μm (REV value at R3). The sample sizes applied in this study are all beyond the smallest representative volumes at each scale, so the images present here are representative at the scales considered in this paper. To assess the representative nature of this data to the well-scale or basin-scale, a larger number of samples could be analysed in the same way and an appropriate upscaling method chosen based on the multi-scale imaging results.

5.2. The pore system within the Bowland Shale studied and implications for gas flow

The pore system of this Bowland Shale sample is primarily within, or associated with, the organic matter. The sample has a small volume of only 0.55 vol % porosity larger than 20 nm and the pore system has extremely low connectivity. The isolated nature of the pores mean that gas transport via the scales considered in this study is unlikely to be important, and the high connectivity of organic and clays provide the potential pathways for gas flow in the alternative forms of diffusion and adsorption-desorption in nano-scale pores within the organic matter (see below).

Fully understanding the pore system is the basis of understanding permeability. The mechanism of gas transport in shale reservoirs can take several forms (for example, Darcy flow, surface
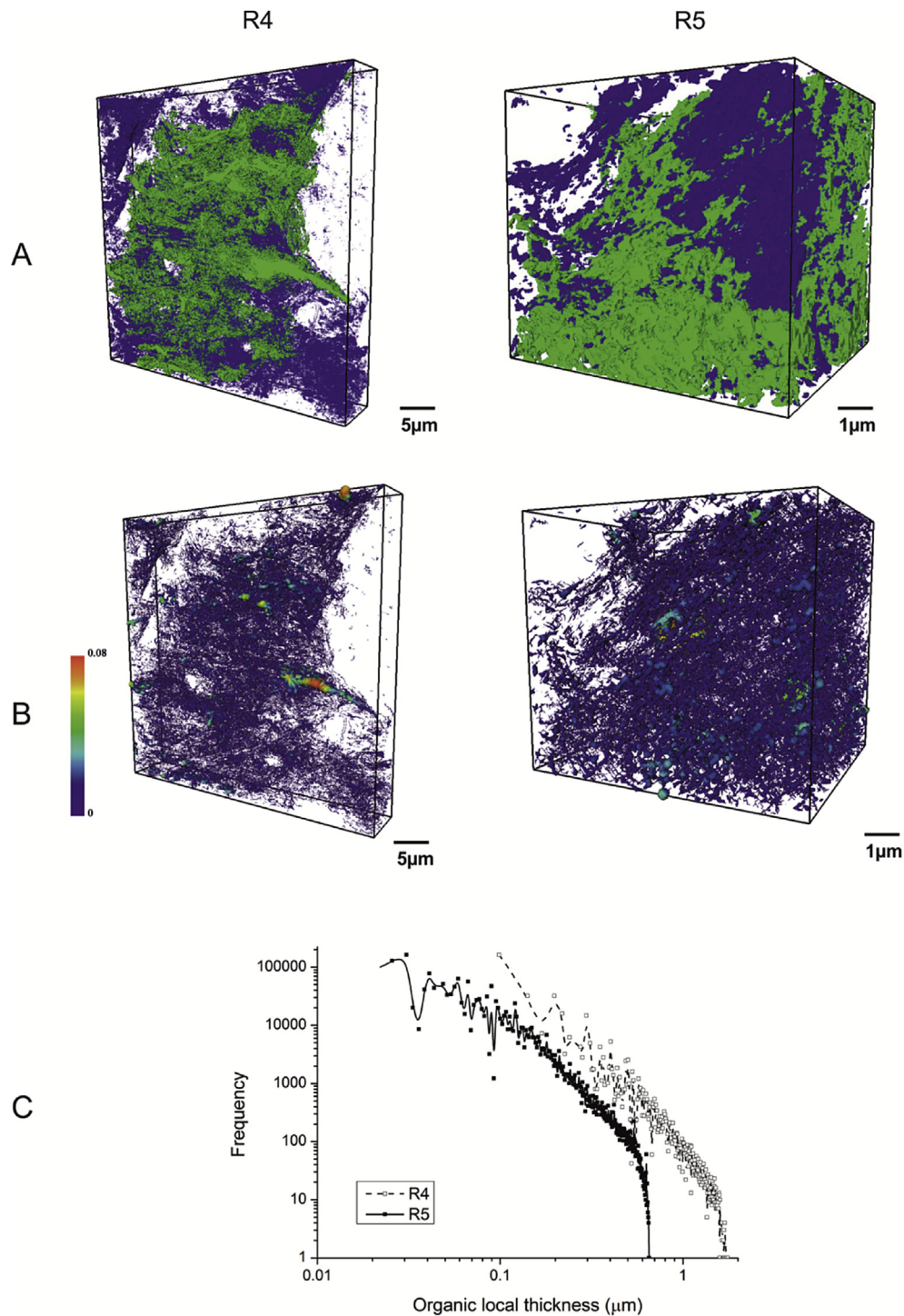
Fig. 9. Organic matter connectivity analysis, showing (A) Connected organic matter and total organic matter distribution in 3D. Green- organic matter connected in Z axis direction. Blue-separated organic matter. (B) Skeletons displayed by the local thickness (the diameter of the largest sphere that fits inside the object and contains the point), colour bar indicating local thickness of organic matter 0—0.08 μm. (C) The distribution of local thickness. (For interpretation of the references to colour in this figure legend, the reader is referred to the web version of this article).

diffusion and molecular diffusion), and each depends on the pore sizes and pore-network size (Javadpour, 2009; Sondergeld et al., 2010). Organic matter particles are likely to be microporous with pores smaller than 6 nm (Rexer et al., 2014), and the surface diffusion within pores combined with molecular diffusion between pores is considered to be the main transport mechanism (Etminan et al., 2014; Mi et al., 2014; Yuan et al., 2014). Organic matter

interface pores observed in this study are separated from other inter-particle pores because of their important function of carrying gas flow from organic source to inorganic matrix. The main mechanism of transport is the adsorption of gas molecules to the pore surface and desorption into pores together with surface diffusion (Javadpour, 2009). The larger volume fractions and more elongate shapes of organic matter interface pores in this sample

provide longer pathways and larger surface area, which provides higher potentials for gas molecule scattering into the mineral matrix. Intra-mineral pores are likely to contribute little to the overall gas transport due to the low connectivity relationship to other pores, while the inter-mineral pores take important roles. Similarly with organic matter interface pores, the large surface area provides potentials for absorbed gas and continuous pathways for pore transport by surface diffusion (Heller et al., 2014; Javadpour, 2009), and the larger percentages and wider distribution of mineral phases allows more gas storage space and transport pathways through whole samples.

In this low-connectivity pore system, the topological properties of porosity outweigh the geometric factors in terms of impacts on fluid flow and future fractured network after fracking (Ewing and Horton, 2002), and smaller penetrating distance between adjacent pores allows easier penetration (Hu et al., 2002) during hydraulic fracturing. Pores with higher local densities are more associated with organic interface pores, indicating secondary fractures may occur at the organic—inorganic interface (Fig. 7). In addition, the easier fracturing direction may be parallel to the bedding plane as this is the preferred pore orientation direction, reducing the distance between adjacent pores. The lower density intra-mineral pores, which are away from organic matter, are unlikely to contribute to gas flow.

No connected pores with equivalent diameter of 20 nm or larger were observed in this sample, and the majority of pores are located at the organic matter—mineral interfaces and between clay minerals. As a result, the connectivity of organic matter and clay minerals becomes particularly important due to the possible presence of other transport forms such as surface diffusion and gas slippage through organic matter and clay minerals. Recent experiments have verified that surface diffusion and gas slippage can occur in organic matter pores where absorbed-gas molecules move along the pore wall, especially for the pores under 100 nm. Knudsen diffusion was suggested to be an important transport mechanism in kerogen (Heller et al., 2014; Javadpour, 2009; Kang et al., 2011; Ren et al., 2015; Zhang et al., 2014), with a much higher contribution to permeability than conventional no-slip flow (Shabro et al., 2014). Although the imaged organic pore size in this study are in the range 20 nm to greater than 1000 nm, there may be pores below 20 nm scattered in the amorphous organic matter (Jiao et al., 2014; Zhang et al., 2014) which are not shown in the imaging due to the limitation of resolution, but their contribution for gas transport cannot be ignored. Apart from the surface diffusion transport for free gas and absorbed gas, the molecular diffusion of dissolved gas through solid organic matter has been shown to happen at the same time (Javadpour, 2009; Mi et al., 2014). Thickness is one important parameter influencing the flow rate and travel time for molecule diffusion (Javadpour et al., 2007), and the low measured value of organic matter local thickness (below 1.8 μm) makes the travelling time short when gas is produced out of organic matter and difference in gas concentration between pore space and inside organic kerogen occurs. Additionally, the high connectivity of organic matter at R4 and R5 provides the possibility of the continuous flow/diffusion transport for gas throughout the whole sample.

Similarly with organic matter, surface diffusion is also speculated to be an important transport mechanism through inorganic matter, especially clay minerals, verified by experiments (Amann-Hildenbrand et al., 2012) and numerical simulation (Sun et al., 2015). Moreover, the larger volume percentage (25%) and higher connectivity (98.94% and 97.66% through the Z axis at R4 and R5 respectively) of clay minerals than organic matter in this sample makes the gas transport via surface diffusion on the margin matrix also possible.

5.3. Comparison to other shale gas reservoirs

Some work has been performed in 3D but still less with the kind of multi-scale approach applied here, and our data allows some comparison between the Bowland Shale and producing reservoirs in North America from a microscopic point of view. Similar pore types, morphologies and distributions have been reported for the highly productive Marcellus and Barnett shales with similar TOC (Loucks et al., 2012; Milliken et al., 2013). For example, elongate or crack-like pores between organic matter and other minerals, irregular or bubble-like pores inside organic matter, and elongate or angular pores between minerals. In terms of organic matter distribution, visual comparison of the published images in these active reservoirs (Curtis et al., 2014; Loucks et al., 2009) with our data suggests similar levels of connectivity. For example, organic matter becomes better connected as the area percentage of organic matter increases from 4.5% to 14.6% in Wolfcamp and Barnett samples in 2D images (Curtis et al., 2014). In the case of the Bowland Shale, the rare, but larger bedding-parallel pores and relatively high silicate and carbonate content (total of ~40 wt %) may both aid recovery during hydraulic fracturing. However, better understanding of the mechanical interaction between the ductile clay minerals (~26 wt%) and enhanced micro-crack formation linked to the high organic content is needed (Sone and Zoback, 2013) before any prediction of ultimate recovery can be attempted.

6. Conclusions

(1) The data presented here shows that combining X-ray computed tomography with serial block surface SEM provides a powerful tool for the multi-scale imaging and quantification of microstructural information in shales, allowing the visualisation of pores, organic matter and inorganic mineral phases over a range of three orders of magnitude (7.7 μm—6.7 nm). The multi-scale approach shows a reasonable correlation to traditional physical and chemistry quantification data. However, it clearly demonstrates increasing heterogeneity at higher resolutions, and the representative of sample sizes at each scale has been confirmed.

(2) The appropriate scales (both field of view and resolution) of specified phases such as pores, organic matter, clay minerals and non-clay minerals were analysed. Characterising the types, size distribution and connectivity of pores required nano-scale resolution, which was also required to analyse the organic matter and clay mineral. The grain sizes and distribution of non-clay minerals can be achieved from submicron-scale above resolution because the maximum field of views at nano resolution did not cover the average grain size of non-clay minerals.

(3) The porosity was classified into four types: 1) intra organic pores, 2) organic interface pores, 3) intra mineral pores and 4) inter mineral pores. Pore size distributions from both nitrogen sorption experiments and 3D imaging correlated well. The pore size frequency distribution displays a primary peak at 40 nm comprised mainly of spherical intra-organic matter pores. A secondary peak at 0.2 μm is mainly made up of elongated inter-particle pores. This secondary peak, although lesser frequency, makes up the bulk of the pore volume in the rock, due to their larger size.

(4) The 20 nm and larger pores imaged did not form visibly-connected flow paths, demonstrating that porous gas flow through this sample cannot be the main transport mechanism. Diffusive transport through the organic matter and clay minerals must also be considered, particularly gas migration

over geological timescales. Specifically, we propose that diffusion between intra-organic matter pores plays an important role in the transfer of gas from the interior of organic matter to its surface. Subsequently, inter-organic matter pores, which dominate pore volumes, transport gas into the inorganic matrix, and the high connectivity of the inter-organic matter and inter-clay mineral pores provides a network for gas storage and for gas transport pathways throughout the whole sample.

Acknowledgements

Appendix A. Supplementary data

Supplementary data related to this article can be found at http://dx.doi.org/10.1016/j.marpetgeo.2016.02.008.

References

Amann-Hildenbrand, A., Ghanizadeh, A., Krooss, B.M., 2012. Transport properties of unconventional gas systems. Mar. Pet. Geol. 31, 90—99.

Ambrose, R.J., Hartman, R.C., Diaz-Campos, M., Akkutlu, Y., Sondergeld, C.H., 2010. New pore-scale considerations for shale Gas in place calculations. In: Petroleum Engineers Unconventional Gas Conference. Society of Petroleum Engineers, Pittsburgh, Pennsylvania.

Andrews, I., 2013. The Carboniferous Bowland Shale Gas Study: Geology and Resource Estimation.

Ausbrooks, R., Hurley, N.F., May, A., Neese, D.G., 1999. Pore-size distributions in vuggy carbonates from core images, NMR, and capillary pressure. In: SPE Annual Technical Conference and Exhibition. Society of Petroleum Engineers, Houston, Texas.

Bai, B., Elgmati, M., Zhang, H., Wei, M., 2013. Rock characterization of Fayetteville shale gas plays. Fuel 105, 645—652.

Bear, J., Braester, C., 1972. On the flow of two immiscible fluids in fractured porous media. Dev. Soil Sci. 2, 177—202.

Borst, R.L., 1982. Some effects of compaction and geological time on the pore parameters of argillaceous rocks. Sedimentology 29, 291—298.

Britt, L., 2012. Fracture stimulation fundamentals. J. Nat. Gas Sci. Eng. 34—51.

Bustin, Bustin, Cui, Ross, Pathi, M., 2008. Impact of shale properties on pore structure and storage characteristics. In: Engineers, S.o.P. (Ed.), SPE Shale Gas Production Conference. Society of Petroleum Engineers, Fort Worth, Texas, USA.

Caplan, J., Niethammer, M., Taylor II, R.M., Czymmek, K.J., 2011. The power of correlative microscopy: multi-modal, multi-scale, multi-dimensional. Curr. Opin. Struct. Biol. 21, 686—693.

Casertano, S., Hut, P., 1985. Core radius and density measurements in N-body experiments connections with theoretical and observational definitions. Astrophys. J. 298, 80—94.

Charsley, T., 1984. Early carboniferous rocks of the swinden I borehole west of Skipton, Yorkshire. Rep. Br. Geol. Surv. 84, 5—12.

Clarkson, Jensen, Chipperfield, 2012a. Unconventional gas reservoir evaluation: what do we have to consider? J. Nat. Gas Sci. Eng. 9—33.

Clarkson, C.R., Solano, N., Bustin, R.M., Bustin, A.M.M., Chalmers, G.R.L., He, L., Melnichenko, Y.B., Radliński, A.P., Blach, T.P., 2013. Pore structure characterization of North American shale gas reservoirs using USANS/SANS, gas adsorption, and mercury intrusion. Fuel 103, 606—616.

Clarkson, C.R., Wood, J., Burgis, S., Aquino, S., Freeman, M., 2012b. Nanopore-structure analysis and permeability predictions for a tight gas siltstone reservoir by use of low-pressure adsorption and mercury-intrusion techniques. SPE Reserv. Eval. Eng. 15, 648—661.

Curtis, M., Ambrose, R., Sondergeld, C., 2010. Structural characterization of gas shales on the micro-and nano-scales. In: Canadian Unconventional Resources and International Petroleum Conference.

Curtis, M.E., Goergen, E., Jernigen, J., Sondergeld, C.H., Rai, C.S., 2014. High-resolution mapping of the distribution and connectivity of organic matter in shales. In: SPE Annual Technical Conference and Exhibition. Society of Petroleum Engineers.

De Pater, C., Baisch, S., 2011. Geomechanical Study of Bowland Shale Seismicity. Synthesis Report.

Dong, Z., Holditch, S., McVay, D., 2013. Resource evaluation for shale gas reservoirs. SPE Econ. Manag. 5, 5—16.

EIA, U., 2015. Annual Energy Outlook 2015. Department of Energy.

Etminan, S.R., Javadpour, F., Maini, B.B., Chen, Z., 2014. Measurement of gas storage processes in shale and of the molecular diffusion coefficient in kerogen. Int. J. Coal Geol. 123, 10—19.

Ewing, R.P., Horton, R., 2002. Diffusion in sparsely connected pore spaces: temporal and spatial scaling. Water Resour. Res. 38, 1285.

Feldkamp, L., Davis, L., Kress, J., 1984. Practical cone-beam algorithm. JOSA A 1, 612—619.

Gawthorpe, R.L., 1987. Tectonosedimentary evolution of the Bowland Basin, N England, during the dinantian. J. Geol. Soc. Lond. 144, 59—71.

Gitman, I.M., Askes, H., Sluys, L.J., 2007. Representative volume: existence and size determination. Eng. Fract. Mech. 74, 2518—2534.

Heath, J.E., Dewers, T.A., McPherson, B.J.O.L., Petrusak, R., Chidsey, T.C., Rinehart, A.J., Mozley, P.S., 2011. Pore networks in continental and marine mudstones: characteristics and controls on sealing behavior. Geosphere 7, 429—454.

Heller, R., Vermylen, J., Zoback, M., 2014. Experimental investigation of matrix permeability of gas shales. AAPG Bull. 98, 975—995.

Hildebrand, T., Rüegsegger, P., 1997. A new method for the model-independent assessment of thickness in three-dimensional images. J. Microsc. 185, 67—75.

Hsieh, J., 2009. Computed tomography: principles, design, artifacts, and recent advances. SPIE 19—36.

Hu, Q., Kneafsey, T.J., Trautz, R.C., Wang, J.S., 2002. Tracer penetration into welded tuff matrix from flowing fractures. Vadose Zone J. 1, 102—112.

Javadpour, F., 2009. Nanopores and apparent permeability of gas flow in mudrocks (shales and siltstone). J. Can. Pet. Technol. 48, 16—21.

Javadpour, F., Fisher, D., Unsworth, M., 2007. Nanoscale gas flow in shale gas sediments. J. Can. Pet. Technol. 46, 55—61.

Jiao, K., Yao, S., Liu, C., Gao, Y., Wu, H., Li, M., Tang, Z., 2014. The characterization and quantitative analysis of nanopores in unconventional gas reservoirs utilizing FESEM—FIB and image processing: an example from the lower Silurian Longmaxi Shale, upper Yangtze region, China. Int. J. Coal Geol. 128—129, 1—11.

Kang, S.M., Fathi, E., Ambrose, R.J., Akkutlu, I.Y., Sigal, R.F., 2011. Carbon dioxide storage capacity of organic-rich shales. SPE J. 16, 842—855.

Ketcham, R.A., Carlson, W.D., 2001. Acquisition, optimization and interpretation of X-ray computed tomographic imagery: applications to the geosciences. Comput. Geosci. 27, 381—400.

Khalili, A.D., Arns, C.H., Arns, J.-Y., Hussain, F., Cinar, Y., Pinczewski, W.V., Latham, S., Funk, J., 2012. Permeability upscaling for carbonates from the pore-scale using multi-scale Xray-CT images. In: SPE/EAGE European Unconventional Resources Conference and Exhibition-from Potential to Production.

Knackstedt, M., Golab, A., Riepe, L., 2012. Petrophysical characterization of unconventional reservoir core at multiple scales. In: SPWLA 53rd Annual Logging Symposium. Society of Petrophysicists and Well-log Analysts.

Korfiatis, P., Skiadopoulos, S., Sakellaropoulos, P., Kalogeropoulou, C., Costaridou, L., 2007. Combining 2D wavelet edge highlighting and 3D thresholding for lung segmentation in thin-slice CT. Br. J. Radiol. 80, 996—1004.

Landis, E.N., Keane, D.T., 2010. X-ray microtomography. Mater. Charact. 61, 1305—1316.

Lang, S., Drouvelis, P., Tafaj, E., Bastian, P., Sakmann, B., 2011. Fast extraction of neuron morphologies from large-scale SBFSEM image stacks. J. Comput. Neurosci. 31, 533—545.

Long, H., Swennen, R., Foubert, A., Dierick, M., Jacobs, P., 2009. 3D quantification of mineral components and porosity distribution in Westphalian C sandstone by microfocus X-ray computed tomography. Sediment. Geol. 220, 116—125.

Loucks, R.G., Reed, R.M., Ruppel, S.C., Hammes, U., 2012. Spectrum of pore types and networks in mudrocks and a descriptive classification for matrix-related mudrock pores. AAPG Bull. 96, 1071—1098.

Loucks, R.G., Reed, R.M., Ruppel, S.C., Jarvie, D.M., 2009. Morphology, genesis, and distribution of nanometer-scale pores in siliceous mudstones of the Mississippian barnett shale. J. Sediment. Res. 79, 848—861.

Lu, J., Ruppel, S.C., Rowe, H.D., 2014. Organic matter pores and oil generation in the Tuscaloosa marine shale. AAPG Bull. 99, 333—357.

Macbeth, C., Hajnasser, Y., Stephen, K., Gardiner, A., 2011. 2011. The effect of mesoseismic shale beds on the reservoir's stress sensitivity to seismic waves. Geophys. Prospect. 59, 90—110, 90—110.

Mi, L., Jiang, H., Li, J., 2014. The impact of diffusion type on multiscale discrete fracture model numerical simulation for shale gas. J. Nat. Gas Sci. Eng. 20, 74—81.

Milliken, K.L., Rudnicki, M., Awwiller, D.N., Zhang, T., 2013. Organic matter—hosted pore system, Marcellus Formation (Devonian), Pennsylvania. AAPG Bull. 97, 177—200.

Pabst, W., Gregorova, E., 2007. Characterization of Particles and Particle Systems. ICT Prague, 2007.

Ren, J., Guo, P., Guo, Z., Wang, Z., 2015. A lattice boltzmann model for simulating gas

flow in kerogen pores. Transp. Porous Media 106, 285—301.

Rexer, T.F., Mathia, E.J., Aplin, A.C., Thomas, K.M., 2014. High-pressure methane adsorption and characterization of pores in Posidonia shales and isolated kerogens. Energy Fuels 28, 2886—2901.

Rokosh, C.D., Pawlowicz, J.G., Berhane, H., Anderson, S.D.A., Beaton, A.P., 2008. What is shale gas? an introduction to shale-gas geology in Alberta. In: Board, E.R.C., Survey, A.G. (Eds.), ERCB/AGS Open File Report 2008—08.

Sakellariou, A., Sawkins, T.J., Senden, T.J., Arns, C.H., Limaye, A., Sheppard, A.P., Sok, R.M., Knackstedt, M.A., Pinczewski, W.V., Berge, L.I., Øren, P.-E., 2003. Micro-CT Facility for Imaging Reservoir Rocks at Pore Scales.

Shabro, V., Kelly, S., Torres-Verdín, C., Sepehrnoori, K., Revil, A., 2014. Pore-scale modeling of electrical resistivity and permeability in FIB-SEM images of organic mudrock. Geophysics 79, D289—D299.

Sok, R.M., Varslot, T., Ghous, A., Latham, S., Sheppard, A.P., Knackstedt, M.A., 2010. Pore scale characterization of carbonates at multiple scales: integration of micro-CT, BSEM, FIBSEM. PetroPhysics 51, 379.

Sondergeld, C.H., Newsham, K.E., Comisky, J.T., Rice, M.C., Rai, C.S., 2010. Petrophysical Considerations in Evaluating and Producing Shale Gas Resources. Society of Petroleum Engineers.

Sondergeld, C.H., Rai, C.S., Curtis, M.E., 2013. Relationship between organic shale microstructure and hydrocarbon generation. In: SPE Unconventional Resources Conference-USA. Society of Petroleum Engineers.

Sone, H., Zoback, M.D., 2013. Mechanical properties of shale-gas reservoir rocks—Part 2: ductile creep, brittle strength, and their relation to the elastic modulus. Geophysics 78, D393—D402.

Stauber, M., Müller, R., 2008. Micro-computed tomography: a method for the non-destructive evaluation of the three-dimensional structure of biological specimens, Osteoporosis. Springer, pp. 273—292.

Sun, H., Chawathe, A., Hoteit, H., Shi, X., Li, L., 2015. Understanding shale gas flow behavior using numerical simulation. SPE J. 20, 142—154.

Thomas, M.M., Clouse, J.A., 1990. Primary migration by diffusion through kerogen: III. Calculation of geologic fluxes. Geochim. Cosmochim. Acta 54, 2793—2797.

Wang, F.P., Reed, R.M., 2009. Pore networks and fluid flow in gas shales. In: Society of Petroleum Engineers Annual Technical Conference and Exhibition, New Oleans, Louisiana.

Waters, C., Jones, N., Collinson, J., Besly, B., 2011. Peak District and North Staffordshire. Geological Society of London.

Wellington, S., Vinegar, H., 1987. X-ray computerized tomography. J. Pet. Technol. 39, 885—898.

Youssef, S., Rosenberg, E., Gland, N., Bekri, S., Vizika, O., 2007. Quantitative 3D characterisation of the pore space of real rocks: improved μ— CT resolution and pore extraction methodology. Int. Sym. Soc. Core Anal. Calg. 1—13.

Yuan, W., Pan, Z., Li, X., Yang, Y., Zhao, C., Connell, L.D., Li, S., He, J., 2014. Experimental study and modelling of methane adsorption and diffusion in shale. Fuel 117, 509—519. Part A.

Zhang, J., Scherer, G.W., 2012. Permeability of shale by the beam-bending method. Int. J. Rock Mech. Min. Sci. 53, 179—191.

Zhang, X., Xiao, L., Shan, X., Guo, L., 2014. Lattice boltzmann simulation of shale gas transport in organic nano-pores. Sci. Rep. 4.